metals

Article

Long-Life Fatigue of Carburized 12Cr2Ni Alloy Steel: Evaluation of Failure Characteristic and Prediction of Fatigue Strength

Hailong Deng *, Qichen Liu, Hang Liu and Huan Yu

College of Mechanical Engineering, Inner Mongolia University of Technology, Hohhot 010051, China; chivalrygreglqc@163.com (Q.L.); lh15647193986@163.com (H.L.); yuhuan111@126.com (H.Y.)

* Correspondence: Denghailong@imut.edu.cn; Tel.: +86-471-657-7339

Received: 22 October 2018; Accepted: 23 November 2018; Published: 1 December 2018

Abstract: In this study, the fatigue failure behaviors of carburized 12Cr2Ni alloy steel were examined in the long-life regime between 10^4 and 10^8 cycles with about 100 Hz under $R = 0$. Results showed that this alloy steel exhibited the double *S-N* characteristics with surface failure and interior failure. From a statistical point of view, the correlation coefficient further proved that the fine granular area (FGA) governed the fatigue performance of carburized 12Cr2Ni alloy steel. Based on the generalized extreme values (GEV) distribution and test data, the predicted maximum defect size was about 23.4 μm. Considering the effect of tensile limit, material hardness, and crack size characteristics, the fatigue strength prediction model under stress ratio of 0 could be established. The predicted fatigue limit for carburized 12Cr2Ni alloy steel at 10^8 cycles under $R = 0$ was 507.86 MPa, and the prediction error of fatigue limit was within 0.04. Therefore, the results were extremely accurate.

Keywords: long-life regime; fracture mechanism; correlation coefficient; maximum inclusion size; fatigue strength

1. Introduction

Due to the higher demand for reliability and safety of mechanical components in industrial design, the fatigue characteristics of structural materials has received increasingly more attention from researchers working on the field of long-life fatigue [1,2]. High carbon [3], Ti-6Al-4V [4], and high-strength alloy steel [5] have been shown to transition between surface failure in short-life region and interior failure in long life region and form typical double *S-N* curves. In the long-life regime, although some factors relating to the fatigue properties of materials have been previously studied, such as load type [6,7], environment [8], defect size [6,9], surface conditions [10,11], and frequency [12], the development of a fatigue strength prediction model has still not been intensively studied.

When the fatigue life is larger than 10^6 cycles, interior-failure mode often occurs in the alloy steel, and its typical characteristic is a fisheye feature on the fracture surface [13]. Approximately in the center of the fisheye, there is an inclusion which original induced fatigue failure [14], and a rough area can be observed around the inclusion [11]. Sakai [3] called this special region fine granular area (FGA). The three stages of the FGA formation process are as follows [15]: (1) grain refinement, (2) coalescence of microcracks, and (3) FGA formation. Over the years, researchers have attempted to explain the FGA formation process in different ways, such as depressive decohesion of spherical carbide [16], hydrogen embrittlement-assisted cracking [17], cyclic compression between crack faces [18], numerous cyclic pressing [19,20], grain refinement and local stress threshold decreasing [21], and nanograin refinement at negative stress effect [2]. The varied theories on the formation of the FGA means the topic needs further study and discussion.

There is, however, one conclusion that all researchers agree to and that is that the FGA governs the long-life behavior of materials. Based on this fact, some fatigue strength prediction models have also been developed [14,22–24]. Murakami [25] et al., for instance, successfully set up a fatigue strength prediction model on the basis of hardness (HV) and defect size. Similarly, other models have looked at growth rate [26], log-log straight line [27], etc. in combination with the defect size. However, although these models can reflect the failure mechanism of materials to a certain extent, they are no longer applicable when the FGA becomes difficult to be observed in the long-life region for some materials.

In this paper, the long-life fatigue performance of carburized 12Cr2Ni alloy steel under $R = 0$ was researched. Using the *S-N* characteristics, failure mechanisms, crack size characteristics, correlation analysis, and stress intensity factor, a fatigue strength prediction model connected with $R = 0$ and with maximum inclusion size is proposed.

2. Experimentation

2.1. Test Specimen and Microstructure

In this research, 12Cr2Ni alloy steel was studied, and its main chemical compositions (mass percentage) were as follows: 0.035 S, 0.60 Mn, 0.035 P, 0.16 C, 0.37 Si, 1.65 Cr, and 3.65 Ni. The carburizing process was carried out in several steps. First, the vacuum furnace was filled with the fresh acetylene gas by a rotary pump at 1 Pa pressure. Then, the specimens were put into the chamber of a vacuum furnace whose pressure was raised to 650 Pa. Next, the furnace was heated to 880 °C and held for 0.5 or 1 h soaking time. The furnace was then heated to the carburizing temperature of about 945 °C and held for 30 min. After the carburizing process, specimens were quenched and tempered as follows: (1) first quenching: 650 °C × 4 h + air cooling; (2) secondary quenching: 800 °C × 3 h + oil cooling; and (3) tempering: 150 °C × 5 h + air cooling.

Using abrasive papers with grits from p600 to p2000, the round-notch surfaces of specimens were gradually polished. The final diameter of the minimum cross section was 4.5 mm, and the surface roughness was about 3.2 μm. The overall structure and dimensions of the fatigue specimen are shown in Figure 1. The stress concentration factor of specimens with an axial-type loading was about 1.02 in this study [28].

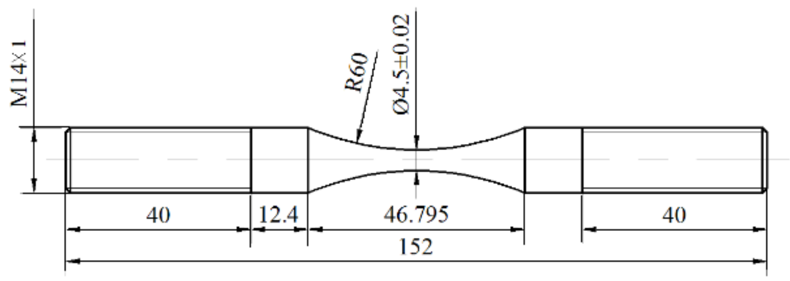

Figure 1. Shape and dimensions of specimen (units: mm).

Scanning electronic microscope (SEM) etched with a 4% alcohol-nitric acid solution was used to observe the microstructures in the carburized layer and the core region, as shown in Figure 2a,b. It was apparent that the acicular martensite, together with partially residual austenites, constituted the microstructures in the carburized layer and that the lattice structure was dense. The microstructures in the core region were mainly the lath martensite. Moreover, using energy-dispersive X-ray spectrometer (EDS), some nonmetallic inclusions with chemical composition of Al_2O_3 could also be found in the microstructure, as indicated in Figure 2c. The other chemical components for inclusions could not be found on the fracture surface. The shear modulus (μ_{inc}) and Poisson's ratio of the inclusion (υ_i) were around 156 GPa and 0.25, respectively [29].

A large electrohydraulic servo torsion fatigue testing machine (MTS 809 which was made by MTS systems Corporation in Eden Prairie, MN, USA) was used for the tensile test. The specifications of the test machine were as follows: maximum axial load 250 kN, maximum torque 2000 N·m, and maximum torsion angle $\pm$ 50°. Using the MTS 809 testing system and five specimens, the tensile strength of carburized 12Cr2Ni alloy steel (σ_b), was measured to be around 1780 MPa.

The nanoindentation test was carried out using the continuous stiffness method (CSM) with Nano Indenter G200. The fixed indentation depth was 2000 nm, and the surface approach velocity was 10 nm/s. The measured value of Vickers hardness was about 613 in the center matrix and about 990 in the surface layer, as shown in Figure 3a, and the depth of the carburized layer was about 1200 μm.

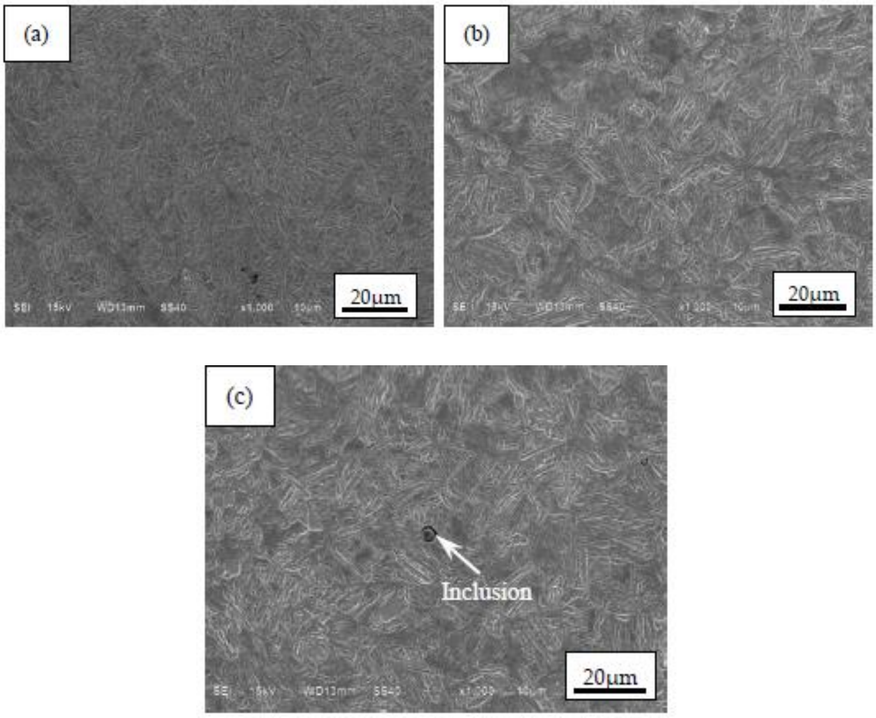

Figure 2. Microstructure observation of carburized 12Cr2Ni alloy steel: (**a**) microstructure in carburized layer; (**b**) microstructure in core region; (**c**) inclusion.

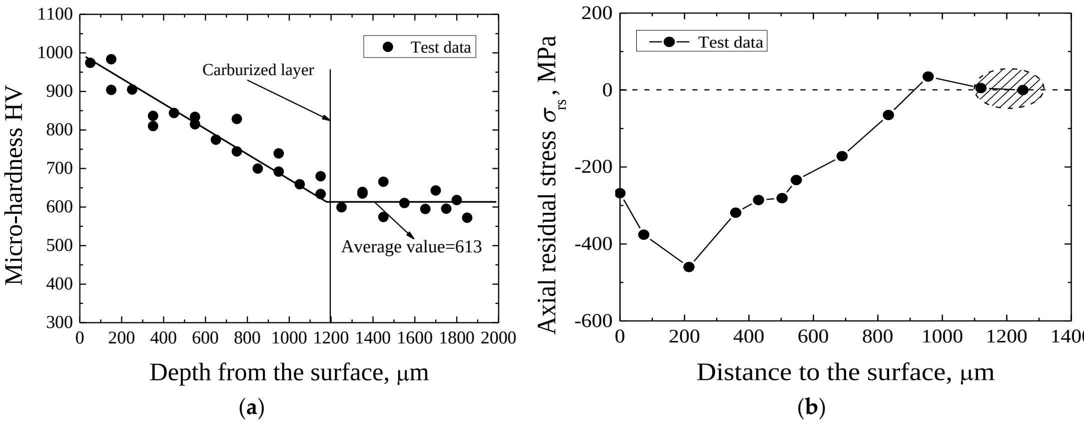

Figure 3. Distribution of microhardness and residual stress: (**a**) distribution of microhardness; (**b**) distribution of residual stress.

Based on electrolytic corrosion and TEC 4000 X-ray diffraction, the distribution of residual stress could be obtained, as shown in Figure 3b. The results showed that as the depth increased, the residual stress decreased first, then increased to the positive stress, and then decreased to 0 MPa. When the depth from the surface was 214 μm, the maximum value of residual compressive stress was about 460 MPa When the depth from surface was near 930 μm, the value of residual stress was greater than 0 MPa, and the maximum residual tensile stress was about 35 MPa. The main reason for this phenomenon is to balance the stress in the radial direction of the specimen. Moreover, when the depth was greater than 1100 µm, the value of residual stress approached 0 MPa, as indicated by the shaded section in Figure 3b. Combined with Figure 3a, the depth of the carburized layer was calculated as about 1200 µm.

2.2. Fatigue Test

At room temperature, the fatigue tests under R = 0 were performed with the axial-type high-frequency fatigue testing machine QBG-100kN (electromagnetic excitation mode) which was made by Changchun Qianbang in Chuangchun of china, and two specimens were tested at each stress level. The loading frequency was about 100 Hz, and the long-life failure regime was between 10^4 and 10^8 cycles. In addition, using the PortixB infrared thermometer, all the specimens were detected, indicating that there was no heating of specimens during the fatigue tests. After completing the long-life fatigue test of the specimens, all the fatigue fracture surfaces were observed with SEM, and the crack initiation position and failure mechanism were analyzed.

3. Results

3.1. S-N Curves

At each stress level, results were obtained for carburized 12Cr2Ni alloy steel under the stress ratio of 0. In addition, a distinct duplex *S-N* curves in the life region between 10^4 and 10^8 cycles could be seen. Figure 4 shows two *S-N* curves plotted to represent the *S-N* characteristics of carburized 12Cr2Ni alloy steel based on different crack growth rates and the least-squares method. The dashed and solid lines show the surface failure and interior failure, respectively. It can be seen that for the surface failure, the surface fatigue limit around the 10^6 cycle was 600 MPa based on the determination of the presence or absence of surface failure mode, as indicated by the shaded section in Figure 4. For the interior failure, the carburized 12Cr2Ni alloy steel showed a continuous decline in *S-N* curves between 10^5 and 10^8 cycles. As the applied stress level at 10^8 cycles was defined as the fatigue strength for failure from interior, $\sigma_{w\text{-}i}$, the value of $\sigma_{w\text{-}i}$ was calculated to be about 490 MPa using fitted lines.

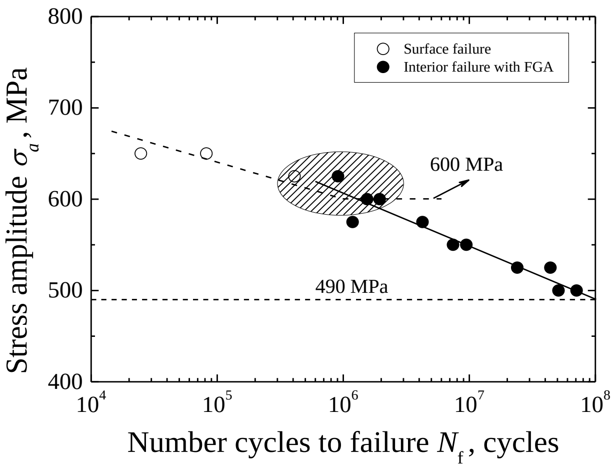

Figure 4. *S-N* curves of carburized 12Cr2Ni alloy steel.

3.2. Failure Fracture Surface and Failure Mechanism

Based on SEM analysis of the initial failure position and the failure mechanism of fracture surfaces in the specimens, the fatigue failure modes could be divided into surface failure and interior failure with FGA for carburized 12Cr2Ni under R = 0.

The interior failure indicated a typical fisheye characteristic, as shown in Figure 5a–c. The features of inclusion-FGA-fisheye could be clearly observed on the fracture surface from inside to outside. The stress concentration caused by the strain inconsistency between the inclusion and the matrix structure led to the failure of the specimen where the source of the crack was a nonmetallic defect. Around the inclusion, a particular rough area, i.e., the fine granular area, could be observed, as shown in Figure 5b. The main reason for the formation of FGA was the crack closure effect associated with plastic deformation and crystal slip under cyclic loading condition. In other words, FGA could be observed even if the stress ratio was 0. However, as the values of the crack closure effect decreased under stress ratio of 0, the morphology of FGA was not as obvious as that under negative stress ratios, as shown in Figure 5c. Outside the fisheye, the surface roughness near the carburized layer side was lower than that in the center. This was because the high hardness in the carburized layer inhibited crack propagation. Based on the characteristics of fracture surface and failure mechanism, the surface of failure specimen could be divided into four areas: (i) inclusion, (ii) FGA, (iii) fisheye, and (iv) momentary fracture area (MFA), as shown in Figure 5a,b.

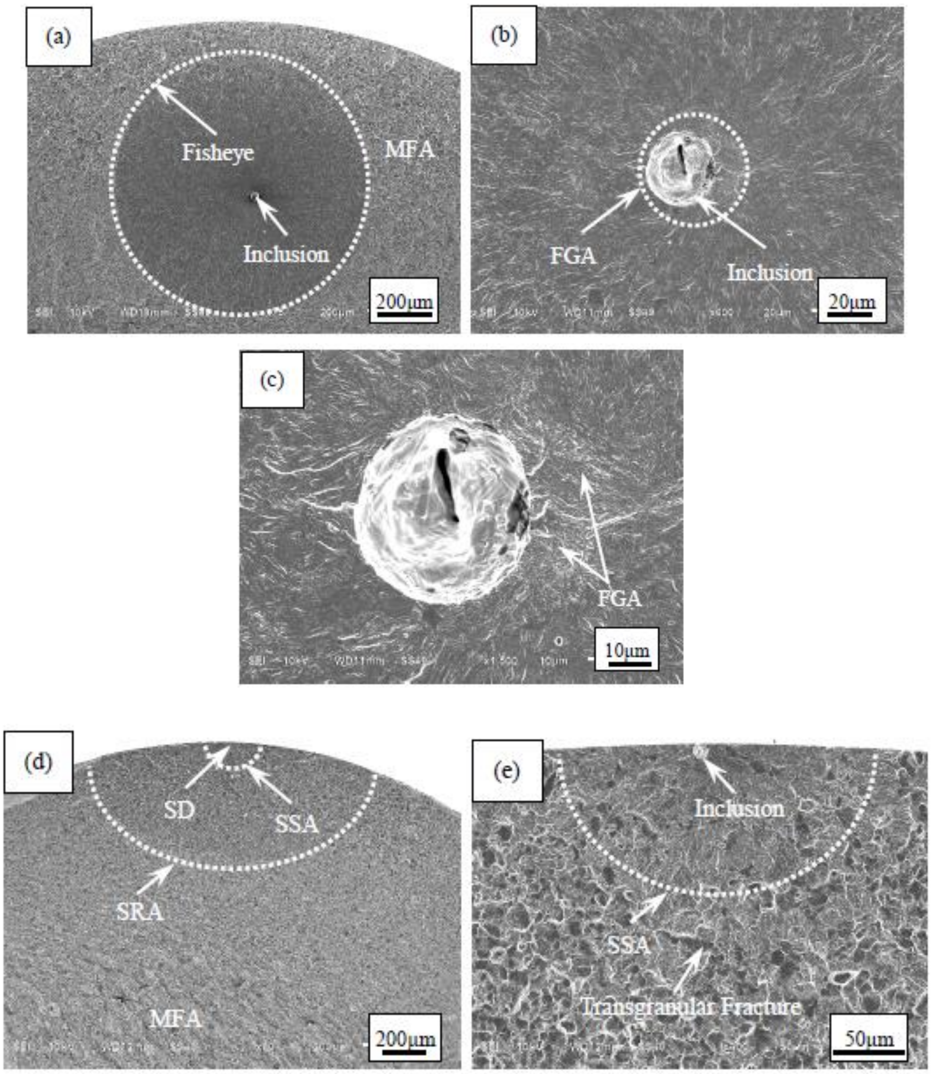

Figure 5. Observation of fatigue fracture surfaces: (**a**) fisheye; (**b**) inclusion with fine granular area (FGA); (**c**) inclusion with FGA at high magnification (σ_a = 575 MPa, N_f = 4,254,700 cycles, R = 0); (**d**) surface-induced failure; (**e**) inclusion (σ_a = 650 MPa, N_f = 82,100 cycles, R = 0).

For the surface failure, the typical semi-arc morphology characteristics could be obtained under R = 0, as indicated in Figure 5d,e. The SD-SSA-SRA feature could be clearly observed on the fracture surface from outside to inside. In the same way, the stress concentration caused by the strain inconsistency between the surface inclusion and the matrix structure led to the failure of specimens where the source of the crack was surface nonmetallic defect. In the SRA, the surface roughness was larger, and transgranular fracture often occurred, as shown in Figure 5e. Outside of the SRA, the fracture surface could be defined as momentary fracture area. As the surface inclusions were all defined as surface defect (SD), and because different crack morphologies in different areas are caused by different crack propagation rates, the entire fracture surface with surface-induced failure could be roughly divided into four areas: (i) SD, (ii) SSA, (iii) SRA, and (iv) MFA, as shown in Figure 5d.

3.3. Evaluation of Crack Characteristic

From the partition of the fracture surface, shown in Section 3.2, the parameter d_{inc} was defined to indicate the depth of interior inclusion from the center to the nearest edge of fracture surface. The variables r_{inc}, r_{FGA}, and r_{fisheye} were used to indicate the radius of inclusion, FGA, and fisheye on the interior fracture surface, respectively. In the same way, r_{SD} and r_{SSA} were used to indicate the radius of SD and SSA on the surface of the fracture surface, respectively.

The distribution between d_{inc} and σ_a are shown in Figure 6. It can be seen that the values of d_{inc} scattered in the range of 506–1765 μm, and some values were larger than the depth of the carburized layer. At high stress levels, the cracks initiated from both the carburized layer and the matrix region. The main reason for this was that the applied maximum stress overcame the high hardness and residual stress in the carburized layer. However, for low-stress regions, the crack mainly initiated from the matrix region, as indicated by the dots in Figure 6. The values of d_{inc} at stress amplitude of 500 MPa were 1135 and 1289 μm.

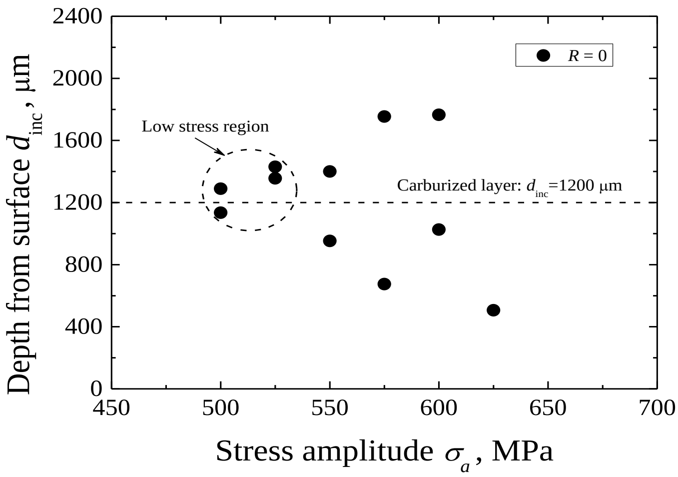

Figure 6. Relationships between the depth of interior inclusion from the center to the nearest edge (d_{inc}) and stress amplitude (σ_a).

From Figure 7, it can be seen that the average value of r_{SD} was 5.9 μm, which was independent of the stress level as denoted by the dashed black line. The main reason for this phenomenon was the machining process, i.e., the number of failure cycles was independent of the inclusion size and depended on the stress level. Moreover, the distribution of the values of r_{SSA} tended to decrease with decreasing fatigue life, as indicated by the solid black line, and the rate of decrease was relatively slow. The values of r_{SSA} scattered in the range of 143.3–163.4 μm.

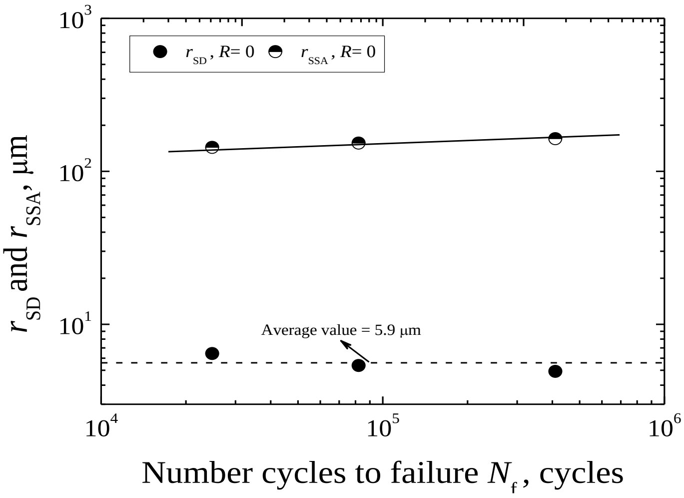

Figure 7. Relationships between radius of surface defect (r_{SD}), radius of surface smooth area (r_{SSA}), and fatigue life (N_f).

The distribution of r_{inc} and r_{FGA} in the long-life region are indicated in Figure 8. Firstly, the values of r_{inc} scattered within the red shaded region, and the average value was about 16.2 μm. The constant size of the inclusion was mostly due to the melting technique, i.e., the size of the inclusion was only related to the melting technique and was independent of stress level. Secondly, the distribution of the values of r_{FGA} all had the tendency to decrease with decreasing N_f, as denoted by the dotted black line within the black shaded region. The values of r_{FGA} scattered in the range of 20.5–28.1 μm. As can be seen from Figure 9, the distribution of the values of $r_{fisheye}$ in the long-life region also had the tendency to decrease with decreasing N_f. The values of $r_{fisheye}$ scattered in the range of 400.9–557.3 μm, and the scatter band was calculated as 1.24 based on the ratio of maximum offset value to mean value of fisheye.

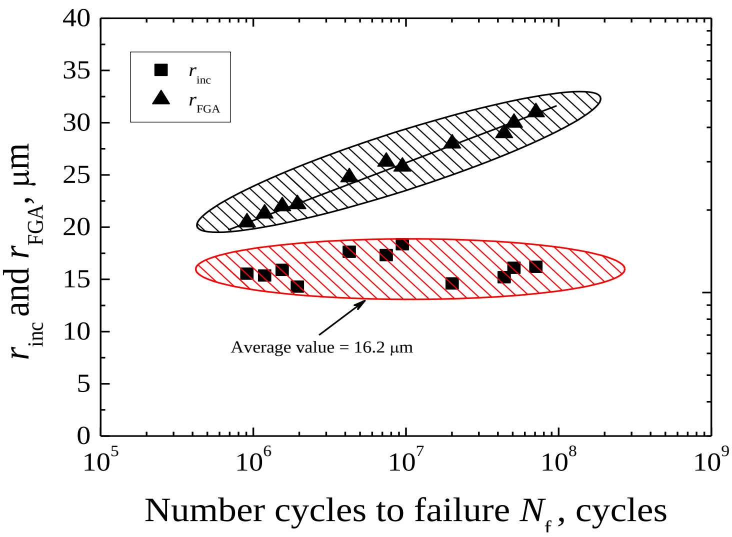

Figure 8. Relationships between radius of inclusion (r_{inc}), radius of FGA (r_{FGA}), and N_f.

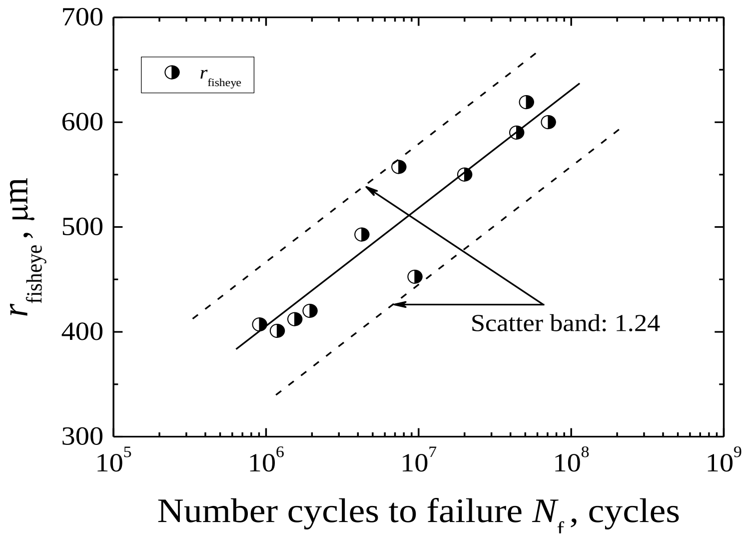

Figure 9. Relationships between radius of fisheye (r_{fisheye}) and N_f.

In order to determine which crack characteristic strongly affected the fatigue life of carburized 12Cr2Ni alloy steels, based on the test data, the correlation coefficient and the statistical significance between the crack characteristic parameters and the final fatigue life, N_f, needed to be first established. In the field of statistics, correlation coefficient, which is described as r_{ij}, can be used to measure the correlation between two variables. The equation can be determined as follows:

$$r_{ij} = \frac{SP_{ij}}{\sqrt{SS_i SS_j}},\ i,j = 1,2,\ldots,m; \quad -1 \geqq r_{ij} \leqq 1 \tag{1}$$

where x_i and x_j are variables, and m is the number of variables. Accordingly, SP_{ij}, SS_i, and SS_j can be expressed as follows:

$$SP_{ij} = \sum (x_i - \overline{x}_i)\left(x_j - \overline{x}_j\right) \tag{2}$$

$$SS_i = (x_i - \overline{x}_i)^2 \tag{3}$$

$$SS_j = \left(x_j - \overline{x}_j\right)^2 \tag{4}$$

where $\overline{x}_i$ and $\overline{x}_j$ are the average values of x_i and x_j, respectively. If $\left|r_{ij}\right| \to 1$, this indicates that the correlation between variables x_i and x_j is stronger. If $\left|r_{ij}\right| \to 0$, this means that there is no correlation.

Furthermore, the statistical significance of the correlation coefficient can be expressed with the following formula:

$$Sig. = \frac{r_{ij}}{\sqrt{\left(1 - r_{ij}^2\right)/(n-2)}},\ df = n - 2 \tag{5}$$

where df and n are the degree of freedom and the number of samples, respectively. The meaning of *Sig.* is significant, and this symbol corresponds to the p-value. If $Sig. \leq 0.05$, this indicates that the correlation coefficient between variables x_i and x_j is significant. If $Sig. \leq 0.01$, this indicates that the correlation coefficient between variables x_i and x_j is strongly significant. If $Sig. > 0.05$, this means that there is no significance between variables x_i and x_j.

Based on Equations (1) and (5), the correlation coefficient and the statistical significance between the crack sizes and fatigue life could be established. The results are indicated in Table 1, which shows the correlation coefficients between r_{inc}, r_{FGA}, r_{fisheye}, and $\text{Log}(N_f)$. We can see that r_{inc} was not related to $\text{Log}(N_f)$ as $Sig. > 0.05$. In the same way, the correlation coefficient between r_{FGA} and $\text{Log}(N_f)$ and r_{fisyeye} and $\text{Log}(N_f)$ were strongly significant as $Sig. \leq 0.01$; the correlation between r_{FGA} and $\text{Log}(N_f)$ was the highest. This proves that the crack initiation behaviors from inclusion to the FGA once again governed the fatigue performance of carburized 12Cr2Ni alloy steels for interior fracture in the long-life region.

Table 1. The correlation coefficient between crack sizes and fatigue life.

Statistical Variable	r_{inc} and Log(N_f)	r_{FGA} and Log(N_f)	$r_{fisheye}$ and Log(N_f)
r_{ij}	0.23	0.995	0.903
Sig.	0.584	0	0.002

3.4. Discussion of Stress Intensity Factor Based on Crack Size

For the interior-failure mode with inclusion-FGA-fisheye characteristic on the fracture surface, these crack characteristic can be used to calculate the stress intensity factor (SIF) [30]. Therefore, SIF ranges at the front of the crack can be written as follows [31]:

$$\Delta K_{\text{inc, or FGA and or fisheye}} = \frac{2}{\pi}\Delta\sigma\sqrt{\pi r_{\text{inc, or FGA and or fisheye}}} \tag{6}$$

where $\Delta\sigma$ is the maximum stress range. For surface failure, the maximum SIF ranges can be given as follows [32]:

$$\Delta K = \frac{1.12\Delta\sigma\sqrt{\pi a}}{E(k)} \cong \Delta\sigma\sqrt{\pi a} \tag{7}$$

Since

$$\frac{E(k)}{1.12} \approx 1 \tag{8}$$

where $E(k)$ is between 1 and $\pi/2$. Thus, ΔK_{SD} and ΔK_{SSA} can be rewritten as follows:

$$\Delta K_{\text{SD and or SSA}} = \Delta\sigma\sqrt{\pi r_{\text{SD or SSA}}} \tag{9}$$

The distribution of ΔK_{inc}, ΔK_{SD}, and ΔK_{FGA} at different stress levels under R = 0 are given in Figure 10. The values of ΔK_{inc} had a tendency to decrease with decreasing stress level between 4.5 and 5.6 MPa·m$^{1/2}$, as indicated by the dashed red line. Similarly, the values of ΔK_{SD} had a tendency to decrease with decreasing stress level between 4.9 and 5.8 MPa·m$^{1/2}$, and the rate of decrease was greater than that of ΔK_{inc}, as indicated by the grey shaded region in Figure 10. According to the fracture mechanics theory, surface fatigue failure will not occur when the surface SIF is lower than a certain value. In this paper, this certain value for carburized 12Cr2Ni alloy steel was 4.9 MPa·m$^{1/2}$, as indicated by the solid black line in Figure 10.

Moreover, the distribution of ΔK_{FGA} was also obtained, as indicated in Figure 10. It was obvious that the value of ΔK_{FGA} was a constant quantity, which was greater than the maximum value of ΔK_{inc}, and the average value was about 6.2 MPa·m$^{1/2}$. This meant that the FGA region could be observed when the maximum SIF of the interior defect was smaller than 6.2. According to the morphology of the FGA region and the tip crack closure effect, a large part of fatigue life is consumed in the formation of FGA. The crack propagation rate in this area is slower, and this area between inclusion and FGA is defined as the small crack initiation stage.

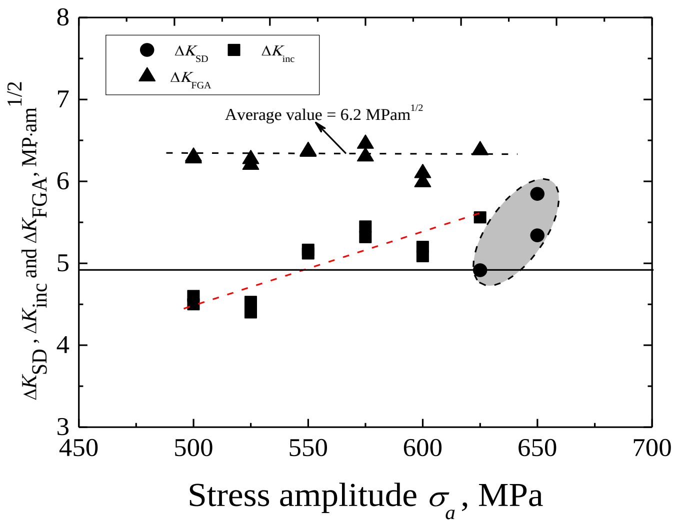

Figure 10. Relationships between stress intensity factor of SD (ΔK_{SD}), stress intensity factor of inclusion (ΔK_{inc}), stress intensity factor of FGA (ΔK_{FGA}) and σ_a.

The relationship between $\Delta K_{fisheye}$, ΔK_{SSA}, and σ_a are indicated in Figure 11. The distribution of $\Delta K_{fisheye}$ and ΔK_{SSA} are indicated in the black shaded region and red shaded region, respectively. It can be seen that these figures were also more or less constant, and the average value was 27.7 MPa·m$^{1/2}$, as indicated by the solid black line. Combined with the theory of fracture mechanics and the morphology of the fracture surface outside of the fisheye or SSA, $\Delta K_{fisheye}$ or ΔK_{SSA} could be indicated as the boundary between the stable crack propagation stage and the rapid crack propagation stage. Above this certain value, the fatigue specimen would quickly fail.

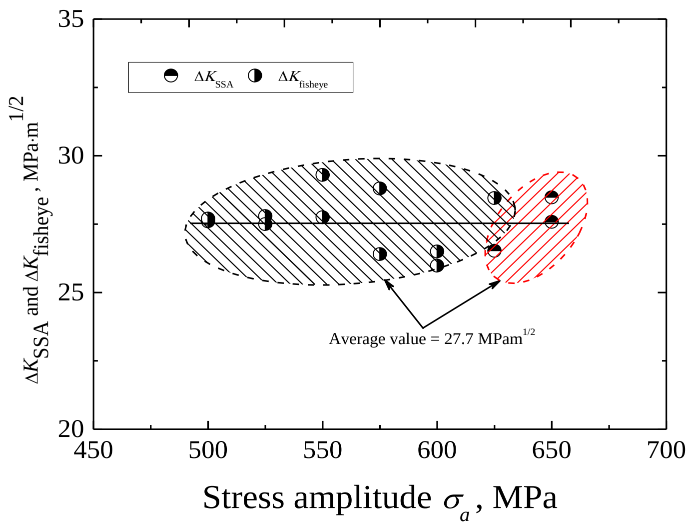

Figure 11. Relationships between stress intensity factor of SSA (ΔK_{SSA}), stress intensity factor of fisheye ($\Delta K_{fisheye}$) and σ_a.

4. Construction of the Fatigue Strength Model

4.1. Evaluation of Maximum Defect Size

The maximum defect size of alloy steel can be calculated using the generalized extreme values (GEV) method during a certain control volume of alloy steel, V (units: mm^3), and when the defect sizes (interior inclusion size) are consistent with the GEV distribution [33]. The cumulative function based on GEV distribution can be expressed as follows:

$$G(x) = \exp\left\{-\left[1+\eta\frac{(x-\lambda)}{\alpha}\right]^{-\frac{1}{\eta}}\right\} \quad (10)$$

where α is scale parameter, λ is location parameter, and η is shape parameter. Based on the equation of mean rank, x_i and y_i can be given as follows:

$$x_i = \lambda - \frac{\alpha}{\eta}y_i \quad (11)$$

$$y_i = 1 - \left[-\ln\left(\frac{i}{N+1}\right)\right]^{-\eta} \quad (12)$$

Based on the linear regression optimization method and the inclusion size data in Figure 12, the value of η was obtained, and the calculated size of η was -0.145. Similarly, the values of α and λ was estimated using the distribution characteristic of the x_i-y_i diagram graph, and the calculated sizes of α and λ were found to be 1.788 and 15.425, respectively.

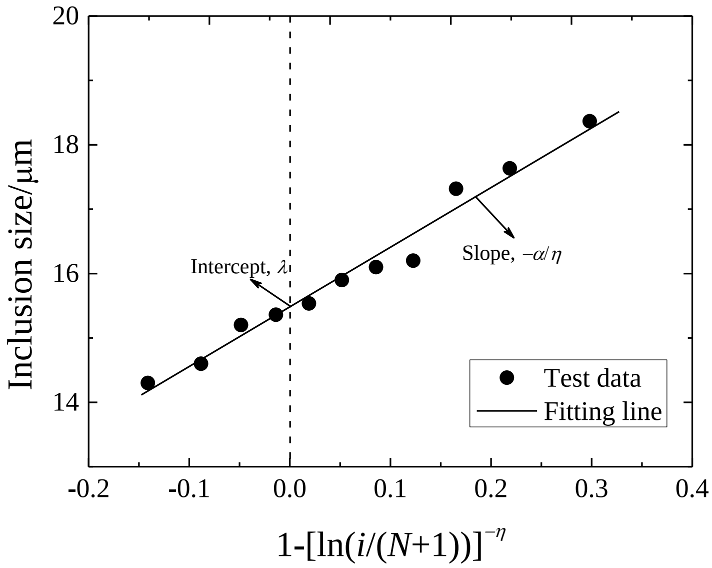

Figure 12. Distribution characteristic of x_i-y_i diagram.

Assuming that the volume of the carburized 12Cr2Ni alloy steel is predicted to be V, the return period can be calculated as follows:

$$T = V/V_0 \quad (13)$$

where

$$V_0 = hS_0 \quad (14)$$

$$h = \left(\sum_i^N x_i\right)/N \quad (15)$$

where V_0 is the volume of the average cross section, S_0 is the minimum area of funnel of the test specimen, and h is the average size of defect. Based on the test data and overall dimension of the specimen, the value of V_0, S_0, and h were 0.257 mm^3, 15.896 mm^2, and 16.159 μm, respectively.

Thus, based on Equations (11) and (12), when the volume is V, the maximum characteristic defect size of the carburized 12Cr2Ni alloy steel can be rewritten as follows:

$$x_V = \lambda - \frac{\alpha}{\eta} y \tag{16}$$

$$y = 1 - \left[-\ln\left(\frac{1}{T}\right) \right]^{-\eta} \tag{17}$$

For the carburized 12Cr2Ni alloy steel, V can be defined as follows [34]:

$$V = 0.25\pi l d^2 \tag{18}$$

where d is the minimum size of funnel of the test specimen, and l is the axial length between the cross sections on both sides where the cross-sectional stress is reduced to 90% of the minimum cross-sectional stress in the axial direction. Based on the simulation, the sizes of d and l were 4.5 mm and 21.3 mm, respectively. Thus, the size of V for the carburized 12Cr2Ni alloy steel was calculated to be about 338.7 mm^3.

The distribution of the maximum defect size versus V for carburized 12Cr2Ni alloy steel is given in Figure 13. The results showed that the defect size had a tendency to decrease with the decrease in V, and the trend gradually approached a certain value. For carburized 12Cr2Ni alloy steel, the maximum defect size ($r_{\text{inc-max}}$) was about 23.4 μm under V = 338.7 mm^3.

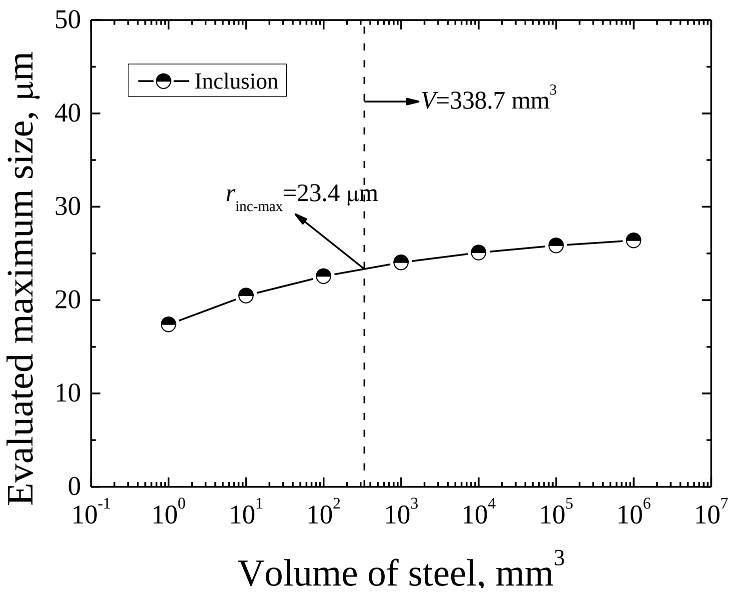

Figure 13. Relationships between defect size and control volume of alloy steel (V).

4.2. Model Construction

It is known that the crack initiation behaviors from inclusion to the FGA governs the fatigue life of carburized 12Cr2Ni alloy steels for interior fracture at low-stress regions. In other words, combined with what is shown in Figures 3 and 6, the fatigue limit of carburized 12Cr2Ni alloy steels was strongly related to the crack initiation life, and the formation of FGA was not affected by residual stress for low-stress region. Even if some inclusions were located in the carburized layer at stress level of 500 MPa, the residual stress at the position of the inclusion was nearly 0 MPa. Thus, the fatigue strength prediction model according to 10^8 cycles could ignore the influence of the residual stress at low-stress region. Moreover, for the high-stress region, the effect of residual stress on fatigue strength is significant and will be further studied in the future.

For interior-failure in high-cycle fatigue regime (10^7 cycle), Murakami [35] proposed a theoretical model to predict the fatigue strength under different stress ratio, and the equation can be written as follows:

$$\sigma_w = 1.56(\mathrm{HV} + 120) / \left(\mathrm{area}^{1/2}\right)^{1/6} ((1 - R)/2)^{\alpha} \quad (19)$$

As area $= \pi r_{\mathrm{inc}}^2$, Equation (19) can be rewritten as follows:

$$\sigma_w = 1.43(\mathrm{HV} + 120) / (r_{\mathrm{inc-max}})^{1/6} ((1 - R)/2)^{\alpha} \quad (20)$$

Therefore, for the fatigue fracture specimen with fatigue limit according to 10^8 cycles, the crack source was mainly located in the core region of the specimen. Thus, the value of HV for 12Cr2Ni alloy steel was 613. As $\alpha = 0.226 + \mathrm{HV} \times 10^{-4}$, the value of α was evaluated to be 0.2873.

Based on Equation (20) and test data of carburized 12Cr2Ni alloy steel, the distribution of σ_w versus V is shown in Figure 14. As can be seen, the variation trend of predicted sizes of σ_w increased with the decrease in V. Compared with Figures 13 and 14, the maximum defect size increased with the increase in V, while the predicted value of σ_w decreased with the increase in V; the variation trend of the two predicted values was just the opposite. This might be because the increase in defect size induced larger stress concentration, while it further reduced fatigue strength of the carburized 12Cr2Ni alloy steel, i.e., the larger the defect size, the lower was the actual fatigue strength. This conclusion is similar to Murakami's model in Reference [35]. Combined with the value of V from Figure 13, the predicted result of the fatigue limit for carburized 12Cr2Ni alloy steel at 10^8 cycles was 507.86 MPa. In contrast to the fatigue strength obtained from the test data by fitted line in Section 3.1, the predicted value of σ_w was a little larger, and the prediction error was within 0.04. This means that even if the potential fatigue strength of carburized 12Cr2Ni alloy steel is improved, the modified model can still be used for fatigue strength prediction under $R = 0$. The accuracy of the prediction of fatigue strength at other stress ratios and specimen shapes will be tested and examined in the future to further validate this model.

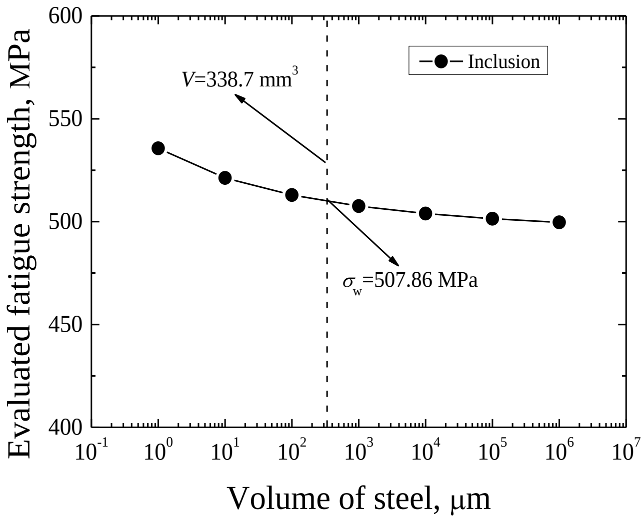

Figure 14. Prediction of fatigue strength for different volumes.

5. Major Conclusions

The major conclusions that can be drawn from the present study are as follows:

1. Surface failure and interior failure in carburized 12Cr2Ni alloy steel showed double *S-N* curves between 10^4 and 10^8, and the fatigue limit was 490 MPa with fitted line.
2. Based on correlation analysis of the fracture surfaces, it was further confirmed that the formation of FGA governed the fatigue performances of carburized 12Cr2Ni alloy steel at low stress levels.

3. Using the GEV method and test data, the defect size was shown to have a tendency to decrease with the decrease in V, and the predicted maximum defect size was calculated as 23.4 μm.
4. Considering the effect of the tensile limit, material hardness, and crack characteristic sizes, a fatigue strength prediction model under stress ratio of 0 was successfully established, and the result was extremely accurate.

Author Contributions: H.D. conceived and designed the experiment; Q.L. and H.L. performed the experiments; H.Y. observed the fracture surfaces; Q.L. analyzed and processed the data; H.D. wrote the paper.

Funding: The authors gratefully appreciate the financial support granted by Natural Science Foundation of Inner Mongolia (No. 2018BS05005), and Foundation Sciences Research Project of Inner Mongolia University of Technology (No. ZZ201801).

Conflicts of Interest: The authors declare no conflict of interest.

Nomenclatures

μ_{inc}	shear modulus of inclusion
υ_i	Poisson's ratio of inclusion
σ_{b}	tensile strength
HV	Vickers hardness
$\sigma_{\text{w-i}}$	fatigue strength for failure from interior
d_{inc}	depth of interior inclusion from the center to the nearest edge
r_{inc}	radius of inclusion
r_{FGA}	radius of FGA
r_{fisheye}	radius of fisheye
r_{SD}	radius of surface defect (SD)
r_{SSA}	radius of surface smooth area (SSA)
N_{f}	fatigue life
r_{ij}	correlation coefficient
x	variable parameter
m	number of variables
$\overline{x}$	average value of x
df	number of degree of freedom
n	number of samples
$\Delta\sigma$	maximum stress range
ΔK_{inc}	stress intensity factor of inclusion
ΔK_{SD}	stress intensity factor of SD
ΔK_{FGA}	stress intensity factor of FGA
$\Delta K_{\text{Fisheye}}$	stress intensity factor of fisheye
ΔK_{SSA}	stress intensity factor of SSA
V	control volume of alloy steel
α	scale parameter
λ	location parameter
η	shape parameter
V_0	volume of average cross section
S_0	minimum area of funnel of test specimen
h	average size of defect
d	minimum size of funnel of test specimen
l	axial length parameter
σ_{m}	mean stress
R	stress ratio
σ_{a}	stress amplitude
σ_{w}	fatigue limit

References

1. Nie, B.; Zhao, Z.; Chen, D.; Liu, S.; Lu, M.; Zhang, J.; Liang, F. Effect of Basketweave Microstructure on Very High Cycle Fatigue Behavior of TC21 Titanium Alloy. *Metals* **2018**, *8*, 401. [CrossRef]
2. Liu, P.; Li, W.; Nehila, A.; Sun, Z.; Deng, H. High Cycle Fatigue Property of Carburized 20Cr Gear Steel under Axial Loading. *Metals* **2016**, *6*, 246. [CrossRef]
3. Sakai, T.; Sato, Y.; Nagano, Y.; Takeda, M. Effect of stress ratio on long life fatigue behavior of high carbon chromium bearing steel under axial loading. *Int. J. Fatigue* **2006**, *28*, 1547–1554. [CrossRef]
4. Günther, J.; Krewerth, D.; Lippmann, T.; Leuders, S.; Tröster, T.; Weidner, A.; Biermann, H.; Niendorf, T. Fatigue life of additively manufactured Ti-6Al-4V in the very high cycle fatigue regime. *Int. J. Fatigue* **2017**, *94*, 236–245.
5. Askari-Paykani, M.; Shahverdi, H.R.; Miresmaeili, R. Fatigue crack growth behavior of a type of novel advanced high-strength steel in a FeCrNiBSi alloy system: A comparison between heat-treated cast and hot-rolled specimens. *Mater. Sci. Eng. A* **2016**, *673*, 280–287. [CrossRef]
6. Li, W.; Sun, Z.; Zhang, Z.; Deng, H.; Sakai, T. Evaluation of crack growth behavior and probabilistic *S-N* characteristics of carburized Cr-Mn-Si steel with multiple failure modes. *Mater. Des.* **2014**, *64*, 760–768. [CrossRef]
7. Shiozawa, K.; Morii, Y.; Nishino, S.; Lu, L. Subsurface crack initiation and propagation mechanism in high-strength steel in a very high cycle fatigue regime. *Int. J. Fatigue* **2006**, *28*, 1520–1532. [CrossRef]
8. Jiang, R.; Everitt, S.; Gao, N.; Soady, K.; Brooks, J.W.; Reed, A.S.P. Influence of oxidation on fatigue crack initiation and propagation in turbine disc alloy N18. *Int. J. fatigue* **2015**, *75*, 89–99. [CrossRef]
9. Berchem, K.; Hocking, M.G. The influence of pre-straining on the high-cycle fatigue performance of two hot-dip galvanised car body steels. *Mater. Charact.* **2007**, *58*, 593–602. [CrossRef]
10. Mahmoudi, A.H.; Ghasemi, A.; Farrahi, G.H.; Sherafatnia, K. A comprehensive experimental and numerical study on redistribution of residual stresses by shot peening. *Mater. Des.* **2016**, *90*, 478–487. [CrossRef]
11. Li, W.; Sun, Z.; Zhang, Z.; Deng, H.; Sakai, T. Influence of case-carburizing and micro-defect on competing failure behaviors of Ni–Cr–W steel under gigacycle fatigue. *Int. J. fatigue* **2015**, *72*, 66–74. [CrossRef]
12. Kovacs, S.; Beck, T.; Singheiser, L. Influence of mean stresses on fatigue life and damage of a turbine blade steel in the VHCF-regime. *Int. J. fatigue* **2013**, *49*, 90–99. [CrossRef]
13. Yang, Z.; Zhang, J.; Li, S.; Li, G.; Wang, Q.; Hui, W.; Weng, Y. On the critical inclusion size of high strength steels under ultra-high cycle fatigue. *Mater. Sci. Eng. A* **2006**, *427*, 167–174. [CrossRef]
14. Liu, Y.; Li, Y.; Li, S.; Yang, Z. Prediction of the *S-N* curves of high-strength steels in the very high cycle fatigue regime. *Int. J. Fatigue* **2010**, *32*, 1351–1357. [CrossRef]
15. Deng, H.; Li, W.; Sakai, T.; Sun, Z. Very High Cycle Fatigue Failure Analysis and Life Prediction of Cr-Ni-W Gear Steel Based on Crack Initiation and Growth Behaviors. *Materials* **2015**, *8*, 8338–8354. [CrossRef]
16. Shiozawa, K.; Lu, L.; Ishihara, S. *S-N* curve characteristics and subsurface crack initiation behaviour in ultra-long life fatigue of a high carbon-chromium bearing steel. *Fatigue Fract. Eng. Mater. Struct.* **2001**, *24*, 781–790. [CrossRef]
17. Murakami, Y.; Yokoyama, N.N.; Nagata, J. Mechanism of fatigue failure in ultralong life regime. *Fatigue Fract. Eng. Mater. Struct.* **2002**, *25*, 735–746. [CrossRef]
18. Nakamura, T.; Oguma, H.; Shinohara, Y. The effect of vacuum-like environment inside sub-surface fatigue crack on the formation of ODA fracture surface in high strength steel. *Proc. Eng.* **2002**, *2*, 2121–2129. [CrossRef]
19. Hong, Y.; Liu, X.; Lei, Z.; Sun, C. The formation mechanism of characteristic region at crack initiation for very-high-cycle fatigue of high-strength steels. *Int. J. Fatigue* **2016**, *89*, 108–118. [CrossRef]
20. Ritz, F.; Stäcker, C.; Beck, T.; Sander, M. FGA formation mechanism for X10CrNiMoV12-2-2 and 34CrNiMo6 for constant and variable amplitude tests under the influence of applied mean loads. *Fatigue Fract. Eng. Mater. Struct.* **2018**, *41*, 1576–1587. [CrossRef]
21. Grad, P.; Reuscher, B.; Brodvanski, A.; Kopnarski, M.; Kerscher, E. Mechanism of fatigue crack initiation and propagation in the very high cycle fatigue regime of high-strength steels. *Scr. Mater.* **2012**, *67*, 838–841. [CrossRef]
22. Akiniwa, Y.; Miyamoto, N.; Tsuru, H.; Tanaka, K. Notch effect on fatigue strength reduction of bearing steel in the very high cycle regime. *Int. J. Fatigue* **2006**, *28*, 1555–1565. [CrossRef]

23. Sun, C.; Xie, J.; Zhao, A.; Hong, Y. A cumulative damage model for fatigue life estimation of high–strength steels in high-cycle and very-high-cycle fatigue regimes. *Fatigue Fract. Eng. Mater. Struct.* **2012**, *35*, 638–647. [CrossRef]
24. Chapetti, M.D.; Tagawa, T.; Miyata, T. Ultra-long cycle fatigue of high-strength carbon steels part II: Estimation of fatigue limit for failure from internal inclusions. *Mater. Sci. Eng. A* **2003**, *356*, 236–244. [CrossRef]
25. Murakami, Y.; Nomoto, T.; Ueda, T. On the mechanism of fatigue failure in the super long life regime ($N > 10^7$ cycles). Part I: Influence of hydrogen trapped by inclusions. *Fatigue Fract. Eng. Mater. Struct.* **2000**, *23*, 893–902. [CrossRef]
26. Tanaka, K.; Akiniwa, Y. Fatigue crack propagation behaviour derived from *S–N* data in very high cycle regime. *Fatigue Fract. Eng. Mater. Struct.* **2002**, *25*, 775–784. [CrossRef]
27. Mayer, H.; Haydn, W.; Schuller, R.; Issler, S.; Bacher-Höchst, M. Very high cycle fatigue properties of bainitic high carbon–chromium steel. *Int. J. Fatigue* **2009**, *31*, 242–249. [CrossRef]
28. Pilkey, W.D.; Pilkey, D.F. *Peterson's Stress Concentration Factors*; John Wiley and Sons Press: New York, NY, USA, 1997.
29. Cerullo, M. Sub-surface fatigue crack growth at alumina inclusions in AISI 52100 roller bearings. *Proc. Eng.* **2014**, *74*, 333–338. [CrossRef]
30. Stephens, R.I.; Fatemi, A.; Stephens, R.R.; Henry, H.O. *Metal Fatigue in Engineering*; A Wiley Interscience: New York, NY, USA, 2001.
31. Marines-Garcia, I.; Paris, P.C.; Tada, H.; Bathias, C.; Lados, D. Fatigue assessment using an integrated threshold curve method–applications. *Eng. Fract. Mech.* **2008**, *75*, 1657–1665. [CrossRef]
32. Marines-Garcia, I.; Paris, P.C.; Tada, H.; Bathias, C. Fatigue crack growth from small to long cracks in very-high-cycle fatigue with surface and internal "fish-eye" failures for ferrite-perlitic low carbon steel SAE 8620. *Mater. Sci. Eng. A* **2007**, *468–470*, 120–128. [CrossRef]
33. Aitkin, M.; Clayton, D. The fitting of exponential, Weibull and Extreme value distributions to complex censored survival data using GLIM. *Appl. Stat.* **1980**, *29*, 156–163. [CrossRef]
34. Murakami, Y. *Metal Fatigue: Effects of Small Defects and Nonmetallic Inclusions*; Elsevier Science: Oxford, UK, 2002.
35. Murakami, Y.; Endo, M. Effect of hardness and crack geometry on delta K threshold of small cracks. *J. Soc. Mater. Sci. Jpn.* **1985**, *35*, 911–917. [CrossRef]